Interlayer magnetic coupling in Fe/MgO junctions characterized by vector magnetization measurements combined with polarized neutron reflectometry

C. Bellouard*
LPM, CNRS–Université Henri Poincaré, 54506 Vandoeuvre-lès-Nancy, France

J. Faure-Vincent
CEA, INAC, SPRAM, LEMOH, F-38054 Grenoble, France

C. Tiusan, F. Montaigne, and M. Hehn
LPM, CNRS–Université Henri Poincaré, 54506 Vandoeuvre-lès-Nancy, France

V. Leiner
Institut für Experimentalphysik/Festkörperphysik, Ruhr-Universität Bochum, D-44780 Bochum, Germany

H. Fritzsche
National Research Council Canada, SIMS, Canadian Neutron Beam Centre, Chalk River Laboratories, Chalk River, Ontario, Canada, K0J 1J0

M. Gierlings
Hahn-Meitner Institut, Glienicker Strasse 100, 14109 Berlin, Germany
(Received 23 July 2008; published 30 October 2008)

Polarized neutron reflectometry has been combined with vector magnetization measurements to analyze the reversal process of antiferromagnetically coupled Fe layers through an insulating MgO spacer. We show that the use of a simple micromagnetic model applied in a field range where the reversal process is reversible allows us to determine separately the magnetic characteristics of the layers such as the anisotropy, bilinear, and biquadratic coupling constants. Using this analysis technique, we can prove that in a Fe(001)/MgO/Fe trilayer with thicknesses 35 nm/0.6 nm/6 nm, the 90° configuration of the Fe layers occurring during the reversal mechanism is only related to the fourfold Fe anisotropy present in both layers without any biquadratic coupling.

DOI: 10.1103/PhysRevB.78.134429 PACS number(s): 75.70.−i, 75.25.+z, 75.50.Bb, 75.60.−d

I. INTRODUCTION

Since the discovery of magnetic coupling between thin layers through a metallic spacer in the Fe/Cr system,[1,2] many studies have been devoted to magnetic coupling in nanostructures. Among the different types of coupling [dipolar or Ruderman-Kittel-Kasuya-Yoshida (RKKY) interaction], the coupling mediated by a tunneling mechanism through an insulating layer[3,4] is the most recent and still puzzling. Because of the very low thickness of the insulating layer (three or four monolayers), the superposition of a quantum tunneling effect with a biquadratic coupling induced by roughness or pinholes cannot be easily ruled out. The difficulty of a clear analysis arises also from the specific magnetic properties of thin magnetic layers (anisotropy and magnetization) which may differ from the bulk ones. Moreover, using only a micromagnetic analysis of coupled thin layers with magnetometry data, the magnetic parameters and the coupling terms are always mixed together, which makes it virtually impossible to determine unambiguously the individual parameters such as anisotropy and coupling terms. However, we show here that by combining polarized neutron reflectometry (PNR) and vector magnetization results, all the energy terms (anisotropy and coupling) can be independently determined.

The epitaxial MgO(001)/Fe/MgO/Fe system is found to exhibit an antiferromagnetic coupling for MgO thicknesses between 0.5 and 1 nm.[3,5] Moreover, the hysteresis loop measured with an applied field along the easy axis (EA) presents a step in a field range between the saturated and the antiferromagnetic states, where the magnetization of the Fe layers forms a right angle.[6,7] The field range of this state can be tuned by structural modifications induced by light ion irradiation.[6] However, the question remains open about the clear origin of this 90° configuration: is it due to a biquadratic coupling or to the fourfold magnetocrystalline anisotropy? In order to answer this question, we focus in the present paper on the micromagnetic behavior of the layers without any assumption concerning the origin of the exchange coupling between the two Fe layers.[8] The magnetization process of a coupled trilayer has been investigated by PNR and vibrating sample magnetometry (VSM) with vector magnetization measurements.

PNR is known to be a powerful tool in investigating the magnetic configuration of coupled multilayers. It has been used to study the oscillatory exchange coupling in Fe/Cr,[9] Co/Cu,[10] or Fe/Nb[11] and the spin-flop transition in Fe/Cr multilayers.[12] PNR can easily prove the antiferromagnetic alignment of magnetic layers separated by nonmagnetic layers because the antiferromagnetic alignment gives rise to an extra peak in the neutron reflectivity curve. Even more complicated structures such as a noncollinear 50° coupling[13] or helical magnetic structures[14] can be determined by PNR.

In the PNR experiments presented here we determined the structural parameters from PNR measurements performed with a field applied along the easy axis in the saturated state. These parameters were then used to simulate the intensities measured with an applied field along the hard axis where the magnetic configuration is not obvious. For an applied field larger than 250 Oe, the reflected intensities can be simulated within the assumption of single domain layers. The neutron experiment then provides the field range where the reversal occurs with coherent rotation and the angles θ_1 and θ_2 of the resulting moment of the two layers with respect to the applied field. On the other hand, the vector magnetization measurement provides the components M_x and M_y that are parallel and perpendicular to the field. In case of a coherent rotation of the layers, these components are the sum of the projections of the total moment of each layer and can be easily expressed as a function of θ_1 and θ_2. The analytical solution of these equations provides two sets of (θ_1, θ_2) values. Thanks to PNR results, the right (θ_1, θ_2) solution can be easily chosen. The PNR experiment allows one then to take full advantage of the vector magnetization measurements, which supply the (θ_1, θ_2) angles in the complete field range where the rotation is coherent.

Moreover, we assume that the total-energy functional of the bilayer can be written in the frame of an analytical Stoner-Wolfarth-type model. The (θ_1, θ_2) solution corresponds then to an equilibrium state which must minimize the total energy. From this condition, the characteristics of the layers such as the fourfold and uniaxial anisotropy constants are determined. The thin layer, deposited on the MgO barrier, is found to obey the same fourfold anisotropy as the thick one, which is close to the bulk iron value. Moreover, this analysis allows one to evaluate the bilinear and the biquadratic couplings independently from the anisotropy terms. Hence, we succeeded in demonstrating that in the investigated sample, the biquadratic coupling is negligible and that the origin of the 90° configuration is only related to the fourfold anisotropy of Fe.

II. SAMPLE PREPARATION AND EXPERIMENTAL DETAILS

The MgO(100)/Fe 35 nm/MgO 0.6 nm/Fe 6 nm/V 70 nm stack has been grown by molecular beam epitaxy. The MgO(001) substrate has been annealed at 500 °C for 15 min. The first Fe layer has been deposited at room temperature using a Knudsen cell at 0.7 nm/min with a chamber pressure of 1×10^{-9} Torr. After deposition, this layer has been annealed at 450 °C for 15 min to smooth its surface up to an atomically flat level. The MgO insulating barrier has been grown using an electron gun after cooling the substrate at 90 °C. Its thickness has been measured with a quartz oscillating sensor after previous calibration using reflection high-energy electron-diffraction (RHEED) intensity.[15] On top of the MgO, a second Fe layer is deposited at 90 °C. Finally a V cap layer is evaporated by an electron gun. The exact Fe and V thicknesses are measured by PNR. The morphology of the MgO layer has been investigated with similar samples by high-resolution transmission electron microscopy.[6,15] The insulating layer appears to be continuous over at least 0.3 μm with smooth interfaces. Moreover, no misfit dislocations within the MgO have been observed for MgO thicknesses lower or equal to 0.8 nm. The MgO layer is strained by the Fe structure with an interplane distance slightly larger than the bulk value.[6]

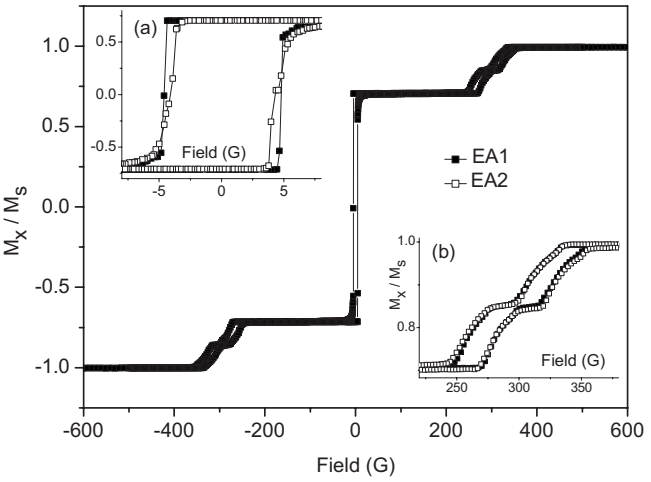

FIG. 1. Normalized magnetization loop measured along the Fe [100] EA1 at room temperature after correction from the diamagnetic contribution of the substrate (solid squares). The inset (a) focuses on the reversal of the antiparallel stack at low fields for both [100] and [010] in-plane easy axes: EA1 (solid squares) and EA2 (open squares). The inset (b) focuses on the reversal of the thin layer for the same directions.

Magnetization measurements with vector analysis have been performed with a commercial vibrating sample magnetometer (LakeShore). PNR experiments with polarization analysis have been performed on the V6 reflectometer at the Hahn Meitner Institut in Berlin[16] and on the ADAM (Advanced Diffractometer for the Analysis of Materials) reflectometer at the Institute Laue Langevin in Grenoble.[17] All experiments presented in this paper have been performed at room temperature on the same sample with a 20×20 mm^2 surface area for the neutron measurements. For the VSM (performed afterward), it has been reduced to its central part with a 10×10 mm^2 area.

III. RESULTS

A. Magnetization measurements

The magnetization loops, measured along both [100] and [010] easy axes, in the sample plane are presented in Fig. 1. The main loop plotted for the [100] direction shows a three-step reversal process characteristic of an antiferromagnetically coupled system: two steps located around ±300 Oe corresponding to the reversal of the thin layer from the parallel to the antiparallel configuration and a step near zero field attributed to the reversal of the net moment of the antiferromagnetically coupled bilayer.[6] The inset (a) focuses on this last reversal step for the field applied along the [100] and [010] in-plane directions. The slight difference observed for the two axes indicates the existence of a uniaxial anisotropy

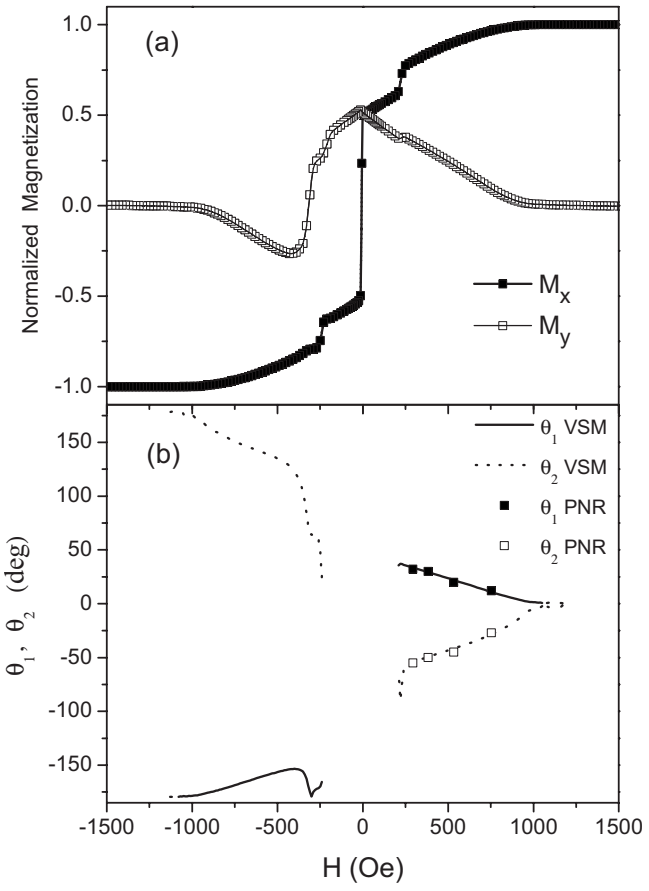

FIG. 2. (a) Hard axis magnetization measurements performed with the VSM. The normalized in-plane magnetizations parallel to the field direction (M_x) and perpendicular to it (M_y) are plotted as a function of the decreasing field. The M_x component has been corrected from the diamagnetic contribution of the substrate. No correction has been done for the M_y component. (b) Solid and dotted lines are θ_1 and θ_2 values deduced from the M_x and M_y components as described in text. The full and open squares show the value estimated from PNR experiments.

superposed to the fourfold one. This feature has already been reported with similar samples and discussed in a previous work.[7] We recall that the deposition geometry is isotropic as the substrate is rotated during growth. This inequivalency of the biaxial crystalline anisotropy has also been observed in Fe/MgO(001) grown by sputtering at normal incidence[18] and has been attributed to surface texture of the MgO substrate. In the following, the easiest axis will be denoted as EA1. The inset (b) focuses on the reversal of the thin layer along the [100] and [010] in-plane directions. No difference is seen for this layer between both easy directions suggesting that only the thick layer is subjected to the uniaxial anisotropy. This inset clearly shows that the reversal of the thin layer occurs in two steps with a net plateau corresponding to a 90° configuration of the layers.

Figure 2(a) presents the field dependence of the normalized M_x (parallel to the field) and M_y (perpendicular to the field) components measured with an applied field along the hard [110] axis. For more clarity, only the part of the loop with decreasing field has been plotted. The M_x component has been corrected from the diamagnetic contribution of the substrate. No correction has been made for the M_y component. EA1 has been rotated counterclockwise from the applied field by $\varphi = +45°$. The positive value of M_y with decreasing field after saturation agrees with an expected rotation of the magnetization toward the EA1 as sketched in Fig. 3. We note that M_y has an asymmetrical shape which evidences an irreversibility that does not appear in the longitudinal M_x component.

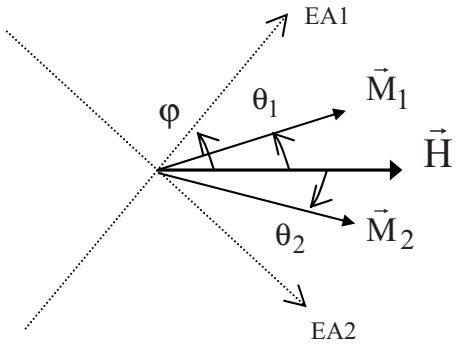

FIG. 3. Sketch of the directions of the magnetic moments $\vec{M}_1$ and $\vec{M}_2$ of the Fe layers with respect to the applied field $\vec{H}$ and magnetocrystalline axis EA1 and EA2.

Assuming a coherent rotation, the angles of the Fe layer magnetizations (θ_1 and θ_2) with respect to the applied field (Fig. 3) can be deduced from the solution of the following equations:

$$\begin{cases} M_x = M_1 \cos\theta_1 + M_2 \cos\theta_2 \\ M_y = M_1 \sin\theta_1 + M_2 \sin\theta_2 \end{cases} \quad (1)$$

as detailed in the Appendix. Two sets of solutions indeed fulfill Eq. (1) when the system is solvable. The choice between both solutions is obvious as only one set of solutions provides opposite sign for θ_1 and θ_2, which is in agreement with PNR measurements presented below. The results are presented in Fig. 2(b) where θ_1 corresponds to the thick layer and θ_2 corresponds to the thin one.

To compare the reversal process between $H > 0$ and $H < 0$, $\theta_1 + 180°$ and $\theta_2 - 180°$ have been plotted as a function of $-H$ in Fig. 4 in addition to θ_1 and θ_2 as a function of H. These plots allow checking the reversibility of magnetization reversal of the layers. The θ_1 and $\theta_1 + 180°$ values corresponding to the thick layer are perfectly superimposed with decreasing field until $H \approx 400$ Oe, whereas no hysteresis is observed for the thin layer until $H \approx 500$ Oe. This result shows that the magnetization reversal appears to be reversible in the thick layer in a larger field window than in the thin one.

B. Polarized neutron reflectivity

Polarized neutron reflectivity with polarization analysis is a suitable technique complementary to macroscopic vectorial magnetometry as it provides a selective depth analysis of the longitudinal and transverse components.[19] The non-spin-flip reflectivities R^{++} and R^{--}, where the neutrons keep their spin

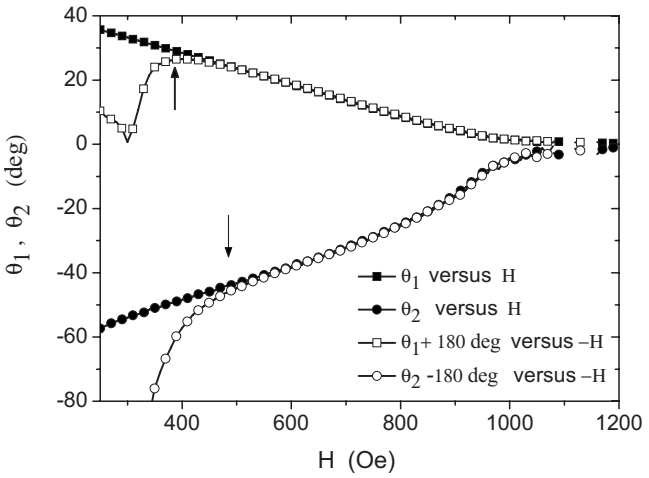

FIG. 4. θ_1 and θ_2 deduced from VSM experiment (performed along the hard axis) plotted versus H, and $\theta_1+180°$ and $\theta_2-180°$ plotted as a function of $-H$. The arrows indicate the reversible limits of the loop.

state, are a function of the magnetic components parallel to the applied field, whereas the spin-flip reflectivities R^{-+} and R^{+-} depend on the transverse magnetic component. More detailed information on the theoretical description of PNR and fitting algorithms can be found elsewhere.[20–22]

Figure 5 presents the non-spin-flip reflectivities measured with a field applied along EA1 for the saturated and antiferromagnetic states, with a field intensity of 900 and 90 G, respectively. In both cases, no spin-flip intensity is detected after polarization efficiency corrections and background subtraction, which is in agreement with perfect collinear alignment of the magnetizations of the layers with respect to the applied field. The structural parameters used for the simulated intensities (PNRSIM software) are reported in Table I.[23] The bulk parameters were used for V and MgO. The same Fe density, close to the bulk one, has been used for both layers. To get a satisfying agreement between simulation and experiment, an additional unknown vanadium oxide VO_x layer has to be introduced; its scattering length density has been tuned to get the best fit.

Figure 6 presents the non-spin-flip and spin-flip reflectivities measured with an applied field along the hard axis with $\varphi=+45°$. When the field is decreased from saturation, a decrease in the gap between R^{++} and R^{--} and a global increase

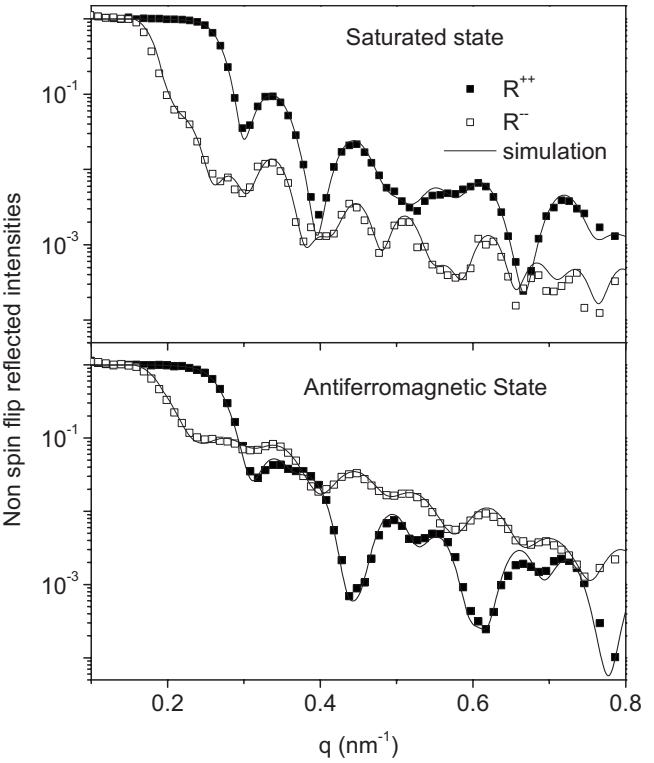

FIG. 5. Non-spin-flip reflectivities R^{++} and R^{--} measured for an applied field of 900 and 90 G along the EA1. These field values correspond to the saturated and the antiferromagnetic states, respectively. The solid lines are simulations.

in R^{+-} are observed. Both features are a signature of a decrease in the longitudinal component and an increase in the transverse one. The simulated intensities (solid line) have been calculated with structural parameters adjusted with easy axis measurements; only the angles θ_1 and θ_2 have been tuned to get the best fit. These values obtained for four field intensities above 250 Oe have been reported in Fig. 2. A good agreement is found with the results deduced from VSM vector analysis. Therefore, the PNR measurements validate the analysis of magnetization measurements in terms of coherent rotation of the moment of the layers giving precise information about the sign of the magnetization angles. The spectra measured for a lower field (240 Oe) cannot be simulated in the assumption of coherent rotation. A formation of domains in the reversal process has then to be taken into

TABLE I. Simulation parameters of the PNR spectra. For the vanadium oxide compound, as the chemical formula is unknown, only the scattering length density has been reported.

	Density (g/cm^3)	Nuclear scattering length density (nm^{-2})	Thickness (nm)	Roughness (nm)	Magnetization (T)
VO_x		4×10^{-8}	3	0.6	
V	6.11	-0.276×10^{-8}	67	0.6	
Fe	7.6	7.7×10^{-8}	5.8	0.6	2.1
MgO	3.58	5.97×10^{-8}	0.6	0.2	
Fe	7.6	7.7×10^{-8}	34.5	0.2	2.1
MgO substrate	3.58	5.97×10^{-8}		0.5	

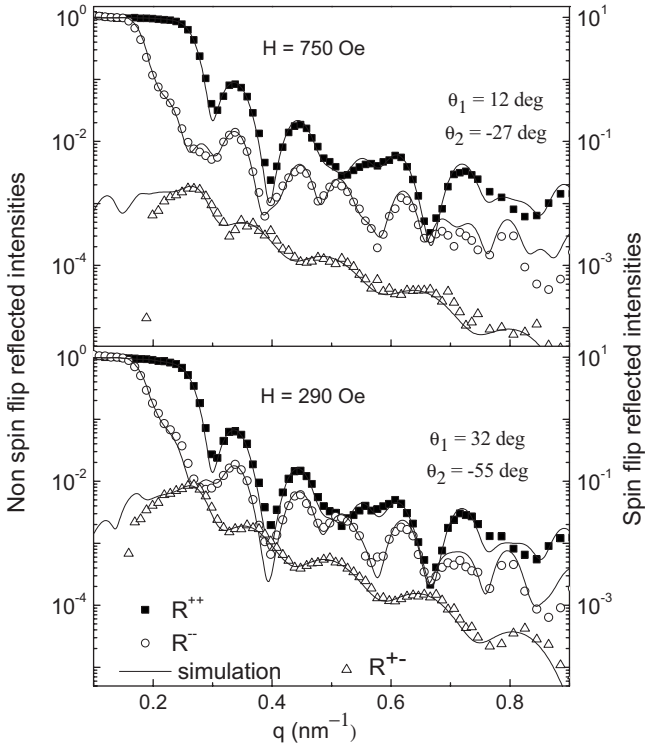

FIG. 6. Non-spin-flip reflectivities R^{++} and R^{--} measured for two fields applied along the hard axis. The spin-flip intensity R^{+-} has been plotted with a translated scale for more clarity. The solid lines are simulations.

account. In the low-field range, the magnetic state is governed by the anisotropy and coupling energy, whereas the Zeeman energy has a stronger contribution in the high-field range. Moreover, fluctuations of the MgO thickness can produce a lateral variation of the coupling which favors the formation of domains. A change of domain structure with applied field has been observed in antiferromagnetically coupled layers using off-specular neutron reflectometry.[24] We note that for $H=+290$ Oe, PNR shows that the reversal is still coherent, although some irreversibility between $H>0$ and $H<0$ appears in the magnetization measurements.

IV. DISCUSSION

In a reversible and coherent reversal process, the magnetic configuration of the layers must minimize the areal energy density

$$E = M_s H(t_1 \cos\theta_1 + t_2 \cos\theta_2) + \frac{K}{4}[t_1 \sin^2 2(\theta_1 - \varphi) + t_2 \sin^2 2(\theta_2 - \varphi)] + k_1 t_1 \sin^2(\theta_1 - \varphi) - J\cos(\theta_1 - \theta_2) - J_b \cos^2(\theta_1 - \theta_2), \quad (2)$$

where M_s is the saturation magnetization of Fe layers with thicknesses t_1 and t_2, J and J_b are the bilinear and biquadratic coupling constants, respectively, K is the cubic anisotropy constant which is assumed to be equal for both layers, φ is the angle of the EA1 axis with respect to the applied field (as sketched in Fig. 3), and k_1 is the uniaxial anisotropy constant present in the thick layer.[25]

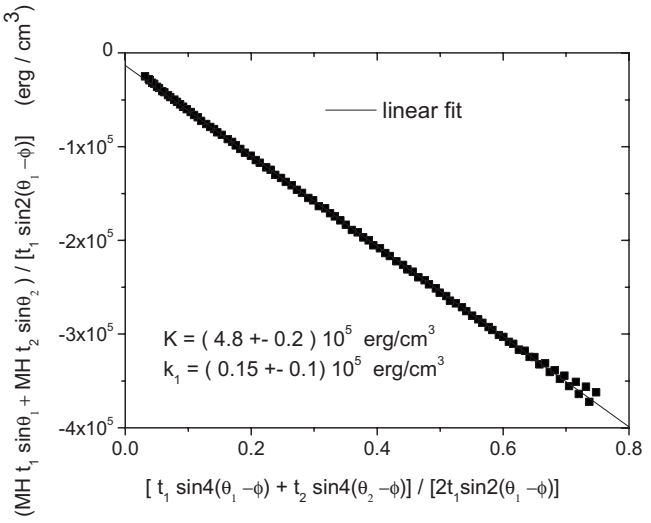

FIG. 7. $\frac{M_S H(t_1 \sin\theta_1 + t_2 \sin\theta_2)}{t_1 \sin 2(\theta_1 - \varphi)}$ versus $\frac{t_1 \sin 4(\theta_1 - \varphi) + t_2 \sin 4(\theta_2 - \varphi)}{2t_1 \sin 2(\theta_1 - \varphi)}$ where t_1 and t_2 are the thicknesses of the Fe layers reported in Table I. M_S is the magnetization of bulk iron, and θ_1 and θ_2 are the angles determined from VSM measurements as described in text with $\varphi=45°$. The positive and negative field ranges are superimposed. The solid line is a linear fit.

The minimization as a function of θ_i: $\frac{\partial E}{\partial \theta_i}=0$ provides two equations,

$$M_S H t_1 \sin\theta_1 + \frac{K t_1}{2}\sin 4(\theta_1 - \varphi) + k_1 t_1 \sin 2(\theta_1 - \varphi) + J\sin(\theta_1 - \theta_2) + J_b \sin 2(\theta_1 - \theta_2) = 0, \quad (3)$$

$$M_S H t_2 \sin\theta_2 + \frac{K t_2}{2}\sin 4(\theta_2 - \varphi) - J\sin(\theta_1 - \theta_2) - J_b \sin 2(\theta_1 - \theta_2) = 0. \quad (4)$$

The sum of these equations provides an expression with only the anisotropy constants K and k_1 which can be written as

$$\frac{M_S H(t_1 \sin\theta_1 + t_2 \sin\theta_2)}{t_1 \sin 2(\theta_1 - \varphi)} = -K\left[\frac{t_1 \sin 4(\theta_1 - \varphi) + t_2 \sin 4(\theta_2 - \varphi)}{2t_1 \sin 2(\theta_1 - \varphi)}\right] - k_1.$$

Figure 7 presents the quantity $\frac{M_S H(t_1 \sin\theta_1 + t_2 \sin\theta_2)}{t_1 \sin 2(\theta_1 - \varphi)}$ as a function of $\frac{t_1 \sin 4(\theta_1 - \varphi) + t_2 \sin 4(\theta_2 - \varphi)}{2t_1 \sin 2(\theta_1 - \varphi)}$ where M_s is the magnetization of bulk iron (in agreement with Table I) and the thicknesses t_1 and t_2 are given by the PNR results (Table I). The field H and angles θ_i are given by VSM results with $\varphi=45°$ in the reversible range of the loop with $H>0$ and $H<0$ as defined in Fig. 4. In Fig. 7, both field ranges are superimposed. The linear fit gives a fourfold anisotropy constant $K=(4.8\pm0.2)\times10^5$ erg/cm^3 close to the bulk value (4.8×10^5 erg/cm^3) and an uniaxial anisotropy constant $k_1=(0.15\pm0.1)\times10^5$ erg/cm^3. The error bar attributed to the

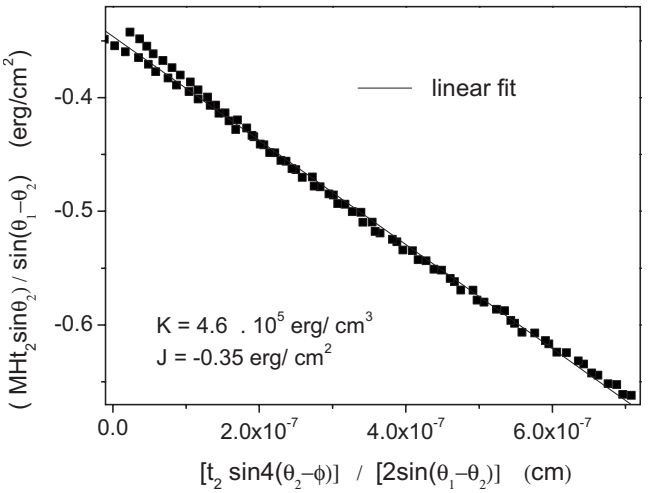

FIG. 8. $\frac{M_S H t_2 \sin\theta_2}{\sin(\theta_1-\theta_2)}$ versus $\frac{t_2 \sin 4(\theta_2-\varphi)}{2\sin(\theta_1-\theta_2)}$ with the same parameters as Fig. 6 (full square). The solid line is a linear fit.

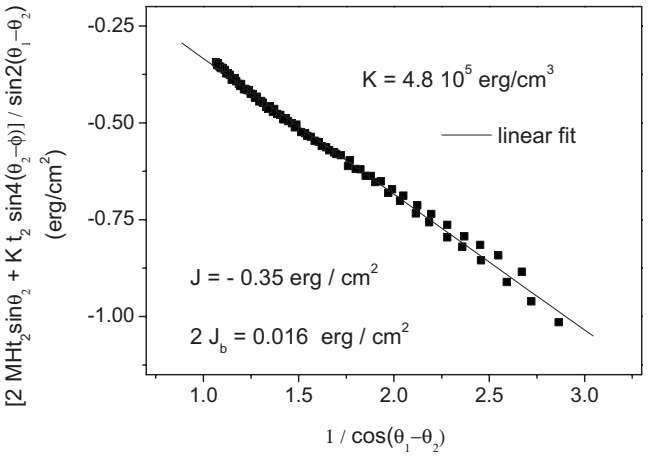

FIG. 9. $2\frac{M_S H t_2 \sin\theta_2}{\sin 2(\theta_1-\theta_2)}+K\frac{t_2 \sin 4(\theta_2-\varphi)}{\sin 2(\theta_1-\theta_2)}$ with the same parameters as Fig. 6 and $K=4.8\times10^5$ erg/cm^3 (full square). The solid line is a linear fit.

anisotropy constants is due to the difficulty of adjusting the $\varphi=45°$ angle. The magnetic properties of Fe films deposited on MgO are known to be thickness dependent: a decrease in the crystalline anisotropy with decreasing thickness L has been indeed observed.[26–29] It has been attributed to a $1/L$ contribution arising from surface anisotropy due to strains induced by the mismatch between film and substrate.[28,29] The recovering of the bulk properties for a 35-nm-thick film agrees with a previous study where the $1/L$ term is found to be smaller for films prepared at 470 K than at room temperature. In the same manner, in our case, the annealing at 450 °C can reduce the distance from the film surface where relaxation occurs.[29]

Equation (4) can be written as

$$\frac{M_S H t_2 \sin\theta_2}{\sin(\theta_1-\theta_2)} = -K\left[\frac{t_2 \sin 4(\theta_2-\varphi)}{2\sin(\theta_1-\theta_2)}\right] + J + 2J_b\cos(\theta_1-\theta_2). \tag{5}$$

The plot of the quantity $\frac{M_S H t_2 \sin\theta_2}{\sin(\theta_1-\theta_2)}$ as a function of $\frac{t_2 \sin 4(\theta_2-\varphi)}{2\sin(\theta_1-\theta_2)}$ presented in Fig. 8 exhibits a linear variation. As a matter of fact, the term with the biquadratic coupling has no weight in Eq. (5). The fit provides $K=(4.6\pm0.2)\times10^5$ erg/cm^3 and $J=-0.35$ erg/cm^2 (-0.35 mJ/m^2). The K value agrees with the preceding result and confirms the assumption made in Eq. (1). This is quite unusual for such a thin Fe layer (5 nm) deposited on MgO where a smaller anisotropy constant is expected as discussed above. We recall that in a previous study, the thickness-dependent term of the Fe magnetic anisotropy has been directly related to the mismatch between Fe(100) and substrate: the ratio of this term between Fe/MgO and Fe/Ag is close to the ratio of the lattice mismatches.[29] In our case, high-resolution transmission electronic microscopy has shown that the MgO 0.6-nm-thick layer is totally strained by the bottom Fe(001) layer without any defect.[6] As a consequence, as no strain is applied to the top Fe layer, it is then reasonable to recover the bulk Fe properties.

The bilinear coupling constant is much larger than that reported by another group[5] but the growth conditions of the sample are clearly different as no annealing of the MgO has been performed in the present study.

Equation (4) can also be written as

$$2\frac{M_S H t_2 \sin\theta_2}{\sin 2(\theta_1-\theta_2)} + K\frac{t_2 \sin 4(\theta_2-\varphi)}{\sin 2(\theta_1-\theta_2)} = J\frac{1}{\cos(\theta_1-\theta_2)} + 2J_b.$$

The linear fit of $2\frac{M_S H t_2 \sin\theta_2}{\sin 2(\theta_1-\theta_2)}+K\frac{t_2 \sin 4(\theta_2-\varphi)}{\sin 2(\theta_1-\theta_2)}$ with $K=4.8\times10^5$ erg/cm^3 as a function of $\frac{1}{\cos(\theta_1-\theta_2)}$ is plotted in Fig. 9. It confirms the negligible weight of the biquadratic term $2J_b=0.016$ erg/cm^2 and provides a slope $J=-0.35$ erg/cm^2.

All the terms of Eq. (2) are then determined. The saturation field measured along the hard axis H_S^h can be calculated from Eqs. (3) and (4) with $J_b=0$ and $k_1\cong0$ in the limit θ_1 and $\theta_2\mapsto0$.

$H_S^d=\frac{2K}{M_s}-\frac{J}{M_s}\left(\frac{1}{t_1}+\frac{1}{t_2}\right)=1000$ Oe (with $K=4.8\times10^5$ erg/cm^3 and $J=-0.35$ erg/cm^2) is in agreement with the magnetization loop plotted in Fig. 2 and with the field dependence of the angles plotted in Fig. 4.

V. CONCLUSION

Polarized neutron reflectivity experiments performed in the hard axis direction allow one to define a field range of the loop where the rotation of the magnetic layers is coherent. The analysis of the vectorial magnetization provides the rotations θ_1 and θ_2 of the layer moments with respect to the applied field. Assuming that it corresponds to an equilibrium state obtained by minimization of the total energy, one can get the anisotropy and coupling constants from the analysis of θ_1 and θ_2 field dependence. We show that both layers follow the fourfold Fe anisotropy with a strong bilinear coupling value of -0.35 ± 0.02 erg/cm^2 and zero biquadratic coupling. Moreover, polarized neutron reflectivity confirms the antiparallel configuration of two epitaxial Fe(001) layers separated by an insulating MgO occurring when the magnetic field is applied along an easy axis.

Beyond the particular results obtained for the Fe/MgO/Fe system, we presented here a useful technique combining po-

larized neutron reflectometry, magnetometry with vector option measurements, and an analytical model. This technique can be used to extract independently the specific magnetic parameters of any other complex coupled bilayer such as the anisotropies and the different orders of coupling.

APPENDIX

Assuming a coherent rotation of two magnetic moments $\vec{M}_1$ and $\vec{M}_2$, the vector magnetization measurement allows one to derive an analytical expression of the angle θ_1 and θ_2 of $\vec{M}_1$ and $\vec{M}_2$ with respect to the field,

$$\begin{cases} M_x = M_1 \cos\theta_1 + M_2 \cos\theta_2 \\ M_y = M_1 \sin\theta_1 + M_2 \sin\theta_2 \end{cases}. \quad \text{(A1)}$$

From these equations, one can deduce

$$\underline{M} = M_x + iM_y = M_1 e^{i\theta_1} + M_2 e^{i\theta_2}, \quad \text{(A2)}$$

$$\underline{M}^* = M_x - iM_y = M_1 e^{-i\theta_1} + M_2 e^{-i\theta_2}, \quad \text{(A3)}$$

where $i^2=-1$.

Using Eq. (A2), $e^{i\theta_2}$ can be expressed as a function of $\underline{M}$ and $e^{i\theta_1}$, and can be replaced in Eq. (A3). A second-order equation as a function of $e^{i\theta_1}$ can then be written as

$$\underline{M}^* M_1 e^{2i\theta_1} + (M_2^2 - M_1^2 - |M|^2) e^{i\theta_1} + \underline{M} M_1 = 0, \quad \text{(A4)}$$

where $|M|^2 = \underline{M}\underline{M}^*$.

This equation has compound number solutions with modulus equal to unity only when its discriminant Δ is negative.

Two couples of solution of Eq. (A1) are then possible,

$$\begin{cases} \cos\theta_1 = \dfrac{M_x A + M_y\sqrt{-\Delta}}{B} \\ \sin\theta_1 = \dfrac{-M_x\sqrt{-\Delta} + M_y A}{B} \end{cases}$$

or

$$\begin{cases} \cos\theta_1 = \dfrac{M_x A - M_y\sqrt{-\Delta}}{B} \\ \sin\theta_1 = \dfrac{M_x\sqrt{-\Delta} + M_y A}{B} \end{cases}$$

with $A = M^2 + M_1^2 - M_2^2$ and $B = 2M_1 M^2$.

$\cos\theta_2$ and $\sin\theta_2$ can then be readily obtained from Eq. (A1). Both set of solutions (θ_1, θ_2) provide the same Zeeman energy for the whole moment (proportional to M_x) and bilinear or biquadratic coupling energy; only the anisotropy term is different.

*bellouar@lpm.u-nancy.fr

[1] P. Grünberg, R. Schreiber, Y. Pang, M. B. Brodsky, and H. Sowers, Phys. Rev. Lett. **57**, 2442 (1986).

[2] M. N. Baibich, J. M. Broto, A. Fert, F. Nguyen Van Dau, F. Petroff, P. Etienne, G. Creuzet, A. Friederich, and J. Chazelas, Phys. Rev. Lett. **61**, 2472 (1988).

[3] J. Faure-Vincent, C. Tiusan, C. Bellouard, E. Popova, M. Hehn, F. Montaigne, and A. Schuhl, Phys. Rev. Lett. **89**, 107206 (2002).

[4] H. Yanagihara, Yuta Toyoda, and Eiji Kita, J. Appl. Phys. **101**, 09D101 (2007).

[5] T. Katayama, S. Yuasa, J. Velev, M. Ye. Zhuravlev, S. S. Jaswal, and E. Y. Tsymbal, Appl. Phys. Lett. **89**, 112503 (2006).

[6] E. Snoeck, P. Baules, G. Ben Assayag, C. Tiusan, F. Greullet, M. Hehn, and A. Schuhl, J. Phys.: Condens. Matter **20**, 055219 (2008).

[7] E. Popova, C. Tiusan, A. Schuhl, F. Gendron, and N. A. Lesnik, Phys. Rev. B **74**, 224415 (2006).

[8] E. Popova, N. Keller, F. Gendron, C. Tiusan, A. Schuhl, and N. A. Lesnik, Appl. Phys. Lett. **91**, 112504 (2007).

[9] A. Schreyer, J. F. Ankner, Th. Zeidler, H. Zabel, M. Schäfer, J. A. Wolf, P. Grünberg, and C. F. Majkrzak, Phys. Rev. B **52**, 16066 (1995).

[10] A. Schreyer, K. Bröhl, J. F. Ankner, C. F. Majkrzak, Th. Zeidler, P. Bödeker, N. Metoki, and H. Zabel, Phys. Rev. B **47**, 15334 (1993).

[11] F. Klose, Ch. Rehm, D. Nagengast, H. Maletta, and A. Weidinger, Phys. Rev. Lett. **78**, 1150 (1997).

[12] K. Temst, E. Kunnen, V. V. Moshchalkov, H. Maletta, H. Fritzsche, and Y. Bruynseraede, Physica B **276-278**, 684 (2000).

[13] A. Schreyer, J. F. Ankner, M. Schäfer, Th. Zeidler, H. Zabel, C. F. Majkrzak, and P. Grünberg, J. Magn. Magn. Mater. **148**, 189 (1995).

[14] G. P. Felcher, W. Lohstroh, H. Fritzsche, M. Münzenberg, H. Maletta, and W. Felsch, Appl. Phys. Lett. **72**, 2894 (1998).

[15] E. Popova, J. Faure-Vincent, C. Tiusan, C. Bellouard, H. Fischer, M. Hehn, F. Montaigne, M. Alnot, S. Andrieu, A. Schuhl, E. Snoeck, and V. da Costa, Appl. Phys. Lett. **81**, 1035 (2002).

[16] F. Mezei, R. Golub, F. Klose, and H. Toews, Physica B **213-214**, 898 (1995).

[17] A. Schreyer, R. Siebrecht, U. Englisch, U. Pietsch, and H. Zabel, Physica B **248**, 349 (1998).

[18] J. L. Costa-Krämer, J. L. Menendez, A. Cebollada, F. Briones, D. Garcia, and A. Hernando, J. Magn. Magn. Mater. **210**, 341 (2000).

[19] J. Meersschaut, C. L'abbé, F. M. Almeida, J. S. Jiang, J. Pearson, U. Welp, M. Gierlings, H. Maletta, and S. D. Bader, Phys. Rev. B **73**, 144428 (2006).

[20] G. P. Felcher, R. O. Hilleke, R. K. Crawford, J. Haumann, R. Kleb, and G. Ostrowski, Rev. Sci. Instrum. **58**, 609 (1987).

[21] S. J. Blundell and J. A. C. Bland, Phys. Rev. B **46**, 3391 (1992).

[22] F. Radu, V. Leiner, M. Wolff, V. K. Ignatovich, and H. Zabel, Phys. Rev. B **71**, 214423 (2005).

[23] The software PNRSIM was developed by U. English for BENSC, Hahn-Meitner-Institut.

[24] D. L. Nagy, L. Bottyan, B. Croonenborghs, L. Deak, B. Degroote, J. Dekoster, H. J. Lauter, V. Lauter-Pasyuk, O. Leupold, M. Major, J. Meersschaut, O. Nikonov, A. Petrenko, R. Rüffer,

H. Spiering, and E. Szilagyi, Phys. Rev. Lett. **88**, 157202 (2002).
[25] B. Heinrich and J. F. Cochran, Adv. Phys. **42**, 523 (1993).
[26] B. Heinrich, Z. Celinski, J. F. Cochran, A. S. Arrott, and K. Myrtle, J. Appl. Phys. **70**, 5769 (1991).
[27] C. Martinez Boubeta, A. Cebollada, J. F. Calleja, C. Contreras, F. Peiro, and A. Cornet, J. Appl. Phys. **93**, 2126 (2003).
[28] Yu. V. Goryunov, G. G. Khaliullin, I. A. Garifullin, L. R. Tagirov, F. Schreiber, P. Bödeker, K. Bröhl, Ch. Morawe, Th. Mühge, and H. Zabel, J. Appl. Phys. **76**, 6096 (1994).
[29] Yu. V. Goryunov, N. N. Garif'yanov, G. G. Khaliullin, I. A. Garifullin, L. R. Tagirov, F. Schreiber, Th. Mühge, and H. Zabel, Phys. Rev. B **52**, 13450 (1995).